AGU PUBLICATIONS

Water Resources Research

TECHNICAL REPORTS: DATA

10.1002/2017WR020832

Quantitative mapping of solute accumulation in a soil-root system by magnetic resonance imaging

S. Haber-Pohlmeier[1], J. Vanderborght[2], and A. Pohlmeier[2]

[1]Institute of Technical and Macromolecular Chemistry, RWTH Aachen University, Aachen, Germany, [2]Agrosphere, IBG-3, Forschungszentrum Jülich, Jülich, Germany

Key Points:
- Longitudinal relaxation time maps allow the quantification of a contrast agent in natural porous media over a wide concentration range
- GdDTPA is a convenient tracer for monitoring flow and for quantification of accumulation processes in a lupin root soil system
- Active and less-active roots can be discriminated

Supporting Information:
- Supporting Information S1
- Data Set S1

Correspondence to:
S. Haber-Pohlmeier,
haber-pohlmeier@itmc.rwth-aachen.de

Citation:
Haber-Pohlmeier, S., J. Vanderborght, and A. Pohlmeier (2017), Quantitative mapping of solute accumulation in a soil-root system by magnetic resonance imaging, *Water Resour. Res.*, *53*, 7469–7480, doi:10.1002/2017WR020832.

Received 8 NOV 2016
Accepted 8 JUL 2017
Accepted article online 13 JUL 2017
Published online 4 AUG 2017

© 2017. American Geophysical Union. All Rights Reserved.

Abstract Differential uptake of water and solutes by plant roots generates heterogeneous concentration distributions in soils. Noninvasive observations of root system architecture and concentration patterns therefore provide information about root water and solute uptake. We present the application of magnetic resonance imaging (MRI) to image and monitor root architecture and the distribution of a tracer, $GdDTPA^{2-}$ (Gadolinium-diethylenetriaminepentacetate) noninvasively during an infiltration experiment in a soil column planted with white lupin. We show that inversion recovery preparation within the MRI imaging sequence can quantitatively map concentrations of a tracer in a complex root-soil system. Instead of a simple T_1 weighting, the procedure is extended by a wide range of inversion times to precisely map T_1 and subsequently to cover a much broader concentration range of the solute. The derived concentrations patterns were consistent with mass balances and showed that the $GdDTPA^{2-}$ tracer represents a solute that is excluded by roots. Monitoring and imaging the accumulation of the tracer in the root zone therefore offers the potential to determine where and by which roots water is taken up.

1. Introduction

Flow and transport processes in soils are heterogeneous. The impact of natural soil heterogeneity and soil structure on flow and transport processes has been a topic of intensive research [*Vereecken et al.*, 2016]. Since plant roots take up a substantial amount of the water that infiltrates at the soil surface, root water uptake is also an important process determining the spatial and temporal variability of water flow and solute transport. The impact of root water uptake and its interaction with spatially variable hydraulic properties on the spatial variability of soil moisture and water fluxes has been investigated at the macroscopic scale, i.e., the scale that does not resolve individual roots, using in situ water content measurement or numerical simulations [*Katul et al.*, 1997; *Hupet and Vanclooster*, 2002; *Teuling and Troch*, 2005; *Kuhlmann et al.*, 2012; *Schlüter et al.*, 2013]. However, the relation between plant water uptake, root distribution, soil properties and soil water states (water content and water potential) needs to be parameterized in these macroscopic approaches. Observations and simulation models that resolve flow and transport processes to individual roots are important to derive parameterizations of macroscopic processes. With respect to transport processes, [*Schroder et al.*, 2012] illustrated using numerical simulations how macroscopic transport is influenced by root water and nutrient uptake processes. Processes around single roots become even more important when water and transport processes are coupled in two directions, for instance due to the impact of osmotic water potentials on root water uptake [*de Jong van Lier et al.*, 2009; *Schroder et al.*, 2014]. These highly spatially resolved simulations require validation by experiments. Furthermore, experimental data about flow and transport processes around and in single roots can be used to derive parameters of the model, for instance root hydraulic parameters [*Zarebanadkouki et al.*, 2016].

Experimental investigations of transport processes around single roots require noninvasive methods with high resolution for concurrent visualization of root systems and their impact on soil variables like water content, water fluxes, and tracer concentrations. Convenient techniques are magnetic resonance imaging (MRI), X-ray computed tomography (X-ray CT) and neutron tomography (NT), which can map roots as well as water content [*Moradi et al.*, 2011; *Daly et al.*, 2015; *Dara et al.*, 2015; *Ahmed et al.*, 2016]. These methods can also be used in combination with tracers (e.g., D_2O for NT [*Zarebanadkouki et al.*, 2012; *Zarebanadkouki et al.*, 2013; *Zarebanadkouki et al.*, 2014] or Iodide for X-ray CT [*Agbogun et al.*, 2013; *Wang et al.*, 2016]).

However, with NT and X-ray CT only relatively high solute concentrations can be visualized. In contrast, MRI can simultaneously image directly water content, root systems, as well as internal structures of roots in the optically opaque soil [*MacFall and Van As*, 1996, *Pohlmeier et al*., 2008; *Segal et al*., 2008; *Nagel et al*., 2009; *Metzner et al*., 2015]. Additionally, uptake pathways or the transport of solutes can be visualized by flow- or tracer imaging. Tracers can be imaged directly using specific resonance frequencies for other nuclei than protons, i.e., X-nuclei NMR which can be used to image for instance lithium [*Harbottle et al*., 2007]. Other tracers are imaged indirectly from their effect on the proton spin density (e.g., D_2O which reduces the proton signal by replacement of water [*Pohlmeier et al*., 2009]), or from their effect on NMR local relaxation times (contrast agents). Contrast agents are often paramagnetic substances that can be imaged at low concentrations [*Oswald et al*., 1997; *Haber-Pohlmeier et al*., 2010; *Moradi et al*., 2010; *Bechtold et al.;* 2011; *Jelinkova et al*., 2011] and are commonly applied in medical diagnostics [*Haake et al*., 1999]. Mostly in MRI the calculation of contrast agent concentrations is based on T_1-weighted spin or gradient echo sequences [*Greiner et al*., 1997, *Morkenborg et al*., 2003; *Nestle et al*., 2003; *Yoon et al*., 2008; *Moradi et al*., 2008b; *Lavini and Verhoeff*, 2010]. These methods are relatively fast, but have a limited accessible concentration range. One of the contrast agents frequently used for medical applications are chelated Gd-complexes due to their high chemical stability and high specific relaxivity.

In preceding papers we applied T_1-weighted MRI image sequences to image $GdDPTA^{2-}$ concentrations in sand columns during transport experiments [*Haber-Pohlmeier et al*., 2010] or solute accumulation during an evaporation experiment [*Bechtold et al*., 2011]. These experiments demonstrated that $GdDPTA^{2-}$ is a stable complex in soil solution and does not adsorb to sand particles. It was furthermore shown that the imaged $GdDPTA^{2-}$ concentration corresponds to the concentration in the pore water and not with the total concentration or mass per bulk volume of porous medium. However, the range of concentrations that could be quantitatively determined was relatively small (0.5 mM to 5 mM) and the relation between the MRI observed signal and the tracer concentration became nonmonotonous at higher concentrations.

The objective of the present study is to investigate the fate of $GdDPTA^{2-}$ in a sand column with a growing and transpiring lupin plant. Therefore, a leaching experiment in the sand column with the lupin plant was carried out. Whether the tracer is excluded from uptake by the roots and whether this exclusion can be quantitatively imaged using MRI were specific questions that were addressed. To achieve this objective we expanded the observable concentration range by mapping the longitudinal relaxation time T_1 from which the concentration is calculated. The proposed imaging technique was validated using calibration phantoms and using mass balances calculations in the soil column.

2. Theory

The theory of MRI is described extensively in the literature [*Callaghan*, 1991; *Blümich*, 2000; *McRobbie et al*., 2007]. Generally, MRI uses the spatially resolved NMR signal, frequently a spin echo, which is encoded in three Cartesian coordinates by switching magnetic field gradients in combination with radio frequency (rf) pulses. After excitation, the signal decays by two different relaxation processes, characterized by the longitudinal relaxation time, T_1, and transverse relaxation time, T_2. In addition to spin density, both relaxation times and experimental parameters like the echo time t_E, the repetition time t_R, or if applicable, a preparation time (see below) control the signal intensity that is recorded in each voxel at the echo time t_E.

The $GdDTPA^{2-}$ tracer influences the T_1 relaxation time of the protons and the following relation between the T_1 relaxation rate ($1/T_1$) and the $GdDTPA^{2-}$ concentrations, c_{Gd}, can be applied:

$$\frac{1}{T_1} = \frac{1}{T_{1,bulk}} + \frac{1}{T_{1,surface}} + a_1 c_{Gd}, \tag{1}$$

where a_1 is the specific relaxivity of $GdDTPA^{2-}$, which is independent of the pore size and saturation [*Haber-Pohlmeier et al*., 2010]. The sum of $1/T_{1bulk}$ and $1/T_{1surface}$ is the longitudinal relaxation rate in absence of $GdDTPA^{2-}$, and can be regarded in good approximation as constant so that its local variation can be neglected versus the third term.

For mapping the T_1 distribution we used a spin echo multislice sequence with inversion recovery preparation for T_1 encoding (IR-SEMS) schematically shown in Figure 1. It uses a Hahn echo, also termed spin echo,

for frequency encoding, phase encoding for the second dimension and slice selection for the third dimension [*Blümich*, 2000; *McRobbie et al.*, 2007].

For a certain repetition time, t_R, and inversion time, t_{inv}, the signal intensity $S(t_{inv},t_R)$ in a given voxel that is observed at the echo time t_E is given by:

$$S(t_{inv},t_R,t_E)=S_0\left(1-2\exp\left(-\frac{t_{inv}}{T_1}\right)\right)\left(1-\exp\left(-\frac{t_R}{T_1}\right)\right)\exp\left(-\frac{t_E}{T_2}\right), \quad (2)$$

where S_0 is proportional to the local spin density that depends on the local water content. In classical T_1 weighted images there is no inversion recovery preparation, which formally corresponds to $t_{inv}=\infty$, and an image of $S(t_R, t_E)$ is obtained. For sufficiently short t_R, the signal is a function of T_1, i.e., "T_1-weighted," and consequently c_{Gd} can be derived [*Haber-Pohlmeier et al.*, 2010]. However, the relation between S/S_0 and c_{Gd} is nonlinear and nonmonotonous. Starting at low c_{Gd}, the signal intensity increases first due to the dominance of the $(1-\exp(-t_R/T_1)$ term. At higher c_{Gd}, the sensitivity to c_{Gd} decreases since the term $\exp(-t_E/T_2)$ becomes dominant and S/S_0 decreases again.

When the repetition time t_R between two successive scans is larger than 5 times T_1, the signal intensity in a voxel is given by the following equation:

$$S(t_{inv})=S_0\left(1-2\exp\left(-\frac{t_{inv}}{T_1}\right)\right)\exp\left(-\frac{t_E}{T_2}\right), \quad (3)$$

The sensitivity of the sequence to T_1 is controlled by the inversion time t_{inv}, i.e., the interval between the initial 180° pulse and the start of the imaging pulse sequence. The dependence of the signal on T_2 relaxation and spatial and temporal variations of spin density S_0 (water content) can be factored out by recording a reference image, S_{ref}, with identical parameters but omitting the inversion pulse, i.e., $t_{inv}=\infty$:

$$S_{ref}=S_0\exp\left(-\frac{t_E}{T_2}\right). \quad (4)$$

Division of equation (3) by equation (4) yields:

$$\frac{S(t_{inv})}{S_{ref}}=\left(1-2\exp\left(-\frac{t_{inv}}{T_1}\right)\right). \quad (5)$$

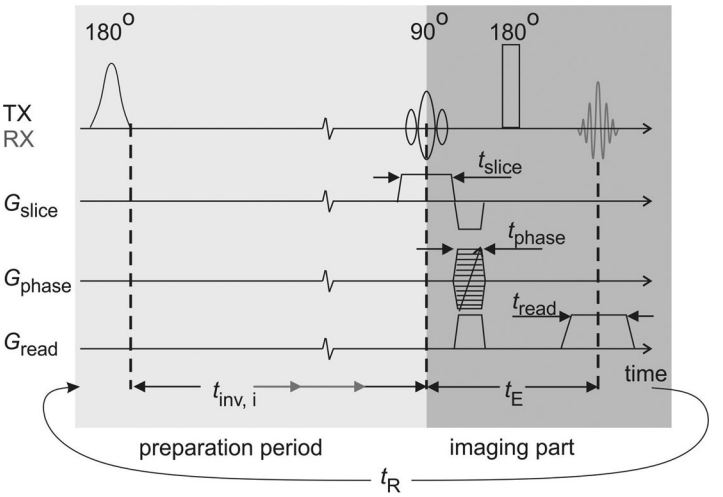

Figure 1. Simplified MRI pulse sequence IR-SEMS (inversion recovery – spin echo multi slice) for Gd-concentration mapping showing in light grey the T_1-encoding preparation period and in medium grey the slice selective spin echo imaging part. The light grey arrows in the preparation period indicate the variation of t_{inv} with different values to sample more data points for a T_1 curve of each voxel. The axes are: TX transmitter, RX receiver, G_{slice} gradient in slice direction (z), G_{phase} gradient in phase encoding direction (y) and G_{read} gradient in frequency encoding direction (x).

By fitting equation (5) to a set of $S(t_{inv})/S_{ref}$ for different t_{inv}, a map of $1/T_1$ is obtained from which c_{Gd} can be calculated directly using equation (1).

Compared to the conventional methods without IR ($t_{inv}=\infty$) and short repetition times t_R to obtain T_1-weighted images, the procedure using IR, full recovery ($t_R \gg T_1$), and reference images has following advantages for determining contrast agent concentration:

1. Cross talk artefacts caused by short t_R are avoided.
2. Normalization on a reference image compensates for inhomogeneities of the radio frequency field for excitation and enhanced T_2 relaxation

at higher Gd concentration, see *Haber-Pohlmeier et al*. [2010, equation (5b)], and for possible local differences in proton density.

3. Direct mapping of $1/T_1$ and the linear relationship between $1/T_1$ and c_{Gd} (equation (1)) widens the accessible concentration range of the contrast agent when compared to the nonlinear and nonmonotonous relation between the T_1 weighted signal and c_{Gd}.

3. Material and Methods

3.1. Calibration Phantom

First, a calibration phantom with different concentrations of $GdDTPA^{2-}$ in sand was investigated to check the accuracy of the procedure. $GdDTPAH_2$ was purchased from Sigma-Aldrich and a stock solution was prepared from which six different test solutions were derived by dilution. The pH was adjusted between 5.5 and 6 to shift the chemical equilibrium to $GdDTPA^{2-}$ (pK_a values are 1.52 and 2.27 for the first and second protonation [*Manning et al*., 1999]). Six cuvettes were filled with natural medium sand (average grain size ca. 0.3 mm, FH31, Quarzwerke Frechen GmbH, Frechen, Germany) and saturated with solutions of $GdDTPA^{2-}$ at 0.0, 0.2, 1.0, 2.0, 3.0, 4.9, and 10.0 mM which covers the expected range in the tracer experiment (see below). They were combined to a bundle and scanned by MRI.

3.2. Plant Setup and Time Line

Lupinus albus was germinated in wet paper and implanted 3 days after germination into a cylindrical Perspex MRI cuvette with a length of 15 cm and an inner diameter of 5 cm. The cuvette was filled 10 cm high with natural medium sand (FH31), the top surface of the soil was covered by coarse sand (grain size ca. 1 mm) as capillary barrier to prevent evaporation from the soil surface, and at the outlet an 11 cm long vertical PVC tube was fixed so that at the lower boundary of the sand packing the suction head was $h = -11$ cm. Bulk density of the sand packing was 1.62 g/cm^3. The plant grew under artificial light in a 12 h/12 h day-night cycle at humidity of about 60% rh. During the growth phase the system was irrigated regularly with N-P-K nutrient solution (0.14 g/kg N, 0.03 g/kg P, 0.08 g/kg K).

The setup and the time-line of the MRI experiment are displayed in Figure 2. Eighteen days after germination we initially imaged the root system architecture and water content and then installed the irrigation head on top, which consists of a circular array of six drip outlets connected to a multichannel tube pump. After 1 day of equilibration with constant irrigation by tap water only, day 0 is defined as the start of the irrigation with 1 mM $GdDTPA^{2-}$ solution. The irrigation rate was adapted when necessary to maintain a constant transpiration-to-efflux ratio (T/E). This readjustment was necessary to compensate for increasing

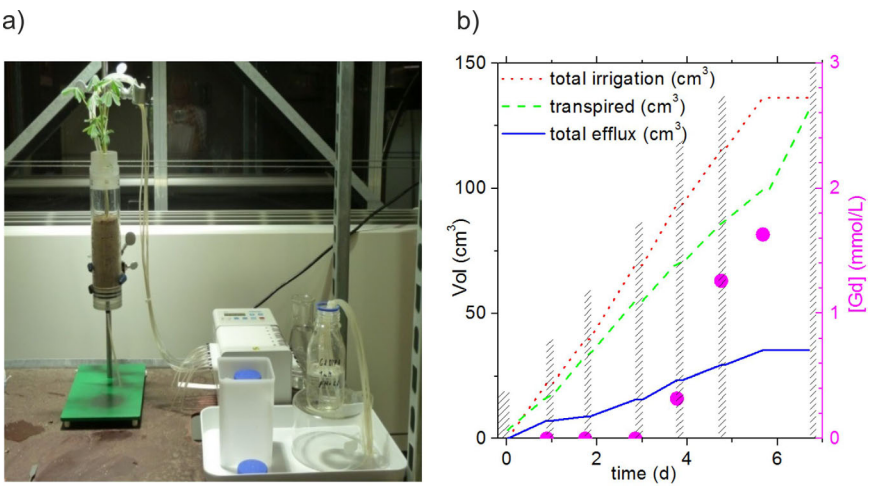

Figure 2. (a) Experimental setup showing (left) the lupin plant in measuring cuvette and irrigation system with multichannel pump and tracer solution with a concentration of 1 mM $GdDTPA^{2-}$. The effluent is collected in 20 mL vials. For the MRI measurements the irrigation was interrupted, the irrigation head removed, and the plant cuvettes was set into the rf-coil of the magnet. (b) Time line of the experiment: day 0 refers to the start of the tracer application which was 19 days after germination. The lines refer to the left ordinate and describe the cumulative volumes of irrigated water (dotted line), transpired water (dashed line), and efflux (full line). On the right ordinate the Gd concentration in effluent is plotted (full circle). Shaded bars indicate the MRI measurement phases with interrupted irrigation and transpiration.

Table 1. Mass Balances During the Experiment

Day	Cumulative Efflux (cm^3)	Cumulative Irrigation (cm^3)	Cumulative Transpiration (cm^3)	θ (cm^3/cm^3)	Gd in Effluent (mM)
0	0	0	0	0.35	0
1	7.2	22.1	16.7	0.35	0
2	8.8	39.6	32.9	0.36	0
3	15.6	69.4	55.0	0.37	0
4	23.4	93.7	70.3	0.37	0.32
5	29.4	115.5	86.1	0.37	1.26
6	35.3	136.2	99.5	0.37	1.63
7	35.3	136.2	131.2	0.22	-
7		*Gd in Plant Parts After Finishing the Experiment*:			
			dry matter	fresh mass	total Gd
		Roots:	5.7 mmol/kg	1.2 mmol/kg	4.1 μmol
		Shoot:	0.19 mmol/kg	0.022 mmol/kg	0.04 μmol
		Leaves:	1.8 mmol/kg	0.35 mmol/kg	0.83 μmol
		Total:			5.0 μmol

transpiration due to plant growth, which is recognizable in Figure 2b after day 2 and day 3. The efflux was collected over the whole day period and c_{Gd} in the effluent was measured by ICP/MS, see Table 1. Each night the irrigation was interrupted, the head was removed and the cuvette was put into the magnet for imaging. It should be noted that instantaneously the efflux stopped too and no transpiration was observed during the scan time, since it was dark inside the magnet.

After 6 days, irrigation was stopped and no further efflux was observed. The plant was left to transpire for one additional day and after 7 days a final MRI scan was performed. Afterward, the plant was excavated and the Gd-content in root system, shoot and leaves were determined.

3.3. Magnetic Resonance Imaging

The samples were scanned in a 1.5 T split-coil MRI scanner (Agilent Technologies) equipped with a 300 mT m^{-1} gradient system and a 10 cm solenoid coil operated by a Varian spectrometer using VNMRJ software. It should be noted that sample diameters are limited by the available rf coil, fitting into the gradient system inside the magnet bore. However, longer columns can be imaged, but it has to be performed zone-wise. The root system architecture was imaged using a T_2-weighted 3D fast spin echo imaging sequence (FSE3D) [*McRobbie et al.*, 2007] with following parameters: field of view (FOV): 60 mm × 60 mm × 70.4 mm, matrix size: 256 × 256 × 64, with resulting physical resolution: 0.234 mm × 0.234 mm × 1.1 mm. The upper surface of the FOV was aligned with the top surface of the sand packing in the column. The reader should note that in MRI this resolution is the real resolution. It is controlled by experimental settings of the pulse sequence parameters like FOV and number of acquired data points. This is recalculated by the pulse program to define the appropriate strength and duration of the magnetic field gradients. Further parameters are $t_E = 20$ ms, $t_R = 2$ s, number of scans: 2, and an echo train length of 32. The total measuring time was 34 min.

The Gd concentration in the liquid phase was imaged using a 2D multislice spin echo sequence with inversion recovery preparation (IR-SEMS, Figure 1). The inversion times were varied in 5 steps with $t_{inv} = 0.02$ s, 0.05 s, 0.15 s, 0.4 s, and 0.6 s. The set of measurements was completed by a reference measurement with identical parameters but no inversion pulse (spin echo multislice sequence, SEMS). For the entire set the FOV was 60 mm × 60 mm, matrix size 256 × 128, slice thickness 2 mm plus 0.2 mm gap, number of slices 40 with the upper slice aligned with the top surface of the sand packing in the column and $t_E = 4$ ms. The repetition time was with 8 s sufficiently long to ensure full recovery, which was checked separately. The total measuring times were about 17 min per inversion time and about 100 min for one set of measurements.

Further data processing comprised zero-filling in phase encoding direction and a 2D Hanning filter in k-space before Fast Fourier transformation, resulting in a resolution of 0.234 mm × 0.234 mm × 2.2 mm for the concentration maps. The images with inversion recovery preparation were normalized on the reference image, and finally T_1 for each voxel was derived by fitting equation (5) to measured $S(t_{inv})/S_{ref}$ for the different t_{inv}. The Gd concentrations were calculated from the resulting T_1 maps using equation (1). All processing

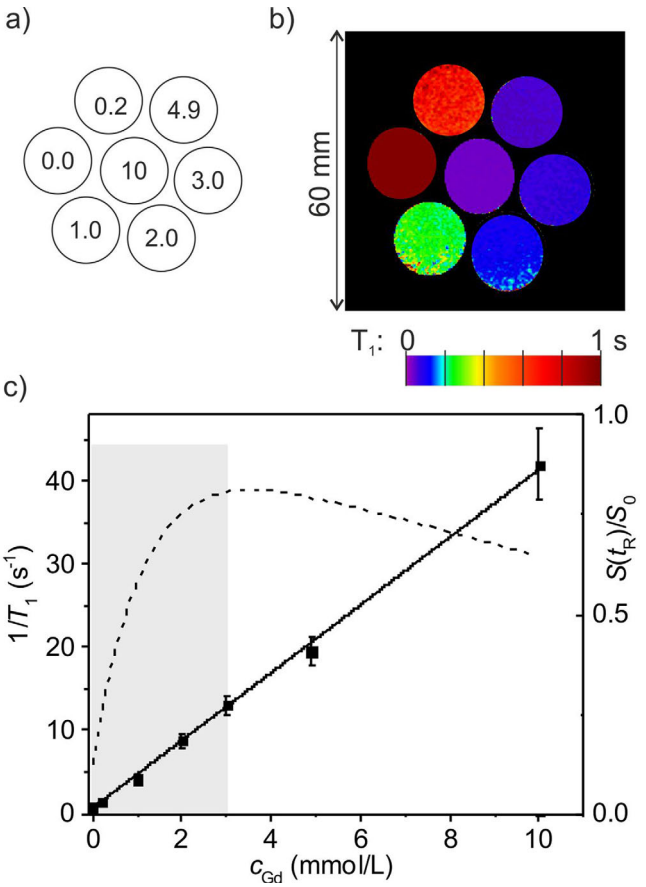

Figure 3. Results for the calibration phantom. (a) Arrangement of the seven glass tubes. The numbers indicate the concentrations of $GdDTPA^{2-}$ in mM. (b) T_1 map. Please note that the scale runs only from 0 to 1 s, so that the tube with 0 mM Gd and T_1 =1.5 s appears overexposed. (c) T_1^{-1} as a function of sample concentrations. The error bars indicate the standard deviation for the different concentrations obtained from regions of interest in Figure 3b. The full line is a linear fit of equation (1). The dashed line indicates the course of $S(t_R)/S_0$, obtained by a T_1-weighted SEMS method with $t_R = 0.2s^{-1}$.

steps of the recorded images, (Fourier transformation, filtering, threshold subtraction, and fitting) were performed offline using IDL (ITT Visual Information Solutions, Boulder, CO).

4. Results and Discussion

4.1. Calibration Phantom

The aim of the first experiment was to demonstrate the reliability of quantitative determination of $GdDTPA^{2-}$ in natural porous media by the procedure described in the Theory section. Figure 3 shows the results for the calibration phantom consisting of six glass-tubes filled with medium sand and saturated with increasing concentrations of Gd. The obtained T_1 map of an exemplary central slice is shown in Figure 3b. By fitting equation (1) to a plot of $1/T_1$ versus c_{Gd}, the parameters $a_1 = 4.0$ $Lmmol^{-1}$ s^{-1} and $(1/T_{1bulk} + 1/T_{1surface}) = 0.66$ s^{-1} are obtained (Figure 3c, full line, left ordinate) which agree very well with the values published in *Haber-Pohlmeier et al*. [2010]. To demonstrate the better performance of this new method we have also included the calculated course of the relative intensity of a T_1-weighted image $S(t_R)/S_0$ for a given short repetition time of $t_R = 0.2$ s (Figure 3c, dashed line, right ordinate). At low concentrations the relative signal intensity increases, then it flattens and finally decreases with increasing c_{Gd}. This flattening and subsequent decrease is due to the increasing contribution of the transverse relaxation term, $\exp(-t_E/T_2)$, in equation (2), which becomes significantly smaller than one for higher Gd concentrations. This procedure allows the determination of Gd only in a narrow concentration range up to approximately 3.0 mM indicated by the shaded area. The advantage of the refined method using T_1-mapping is the elimination of T_2 dependence by the normalization on a reference image and the linear relation between $1/T_1$ and the concentration that allows covering a much larger concentration range. In our calibration experiments, the largest concentration considered was 10 mM corresponding to a T_1 relaxation time of 0.025 s which still gave a detectable signal S/S_{ref} for a t_{inv} of 0.02 s. According to technical specifications of the MRI scanner, t_{inv} can be reduced to 0.005 s which allows according to equations (5) and (1) the detection of c_{Gd} up to 50 mM. For the lowest concentration that we considered, 0.2 mM, the noise in $1/T_1$ in the calibration sample was 0.13. Using equation (1), this noise in $1/T_1$ corresponds to a noise in the concentrations of 0.033 mM. This is still considerably smaller than 0.2 mM so that a concentration of 0.2 mM can be quantified. This extended concentration range opens the possibility to observe transport and enrichment processes over a larger range of concentrations.

4.2. Tracer Transport in Lupin Sand System

Four days after the start of the tracer application, the breakthrough of Gd was detected in the efflux, see Figure 2. After 6 days the irrigation was stopped, resulting in an instantaneous termination of the efflux, see Figure 2b. Since the transpiration continued, the water content decreased during the following day from

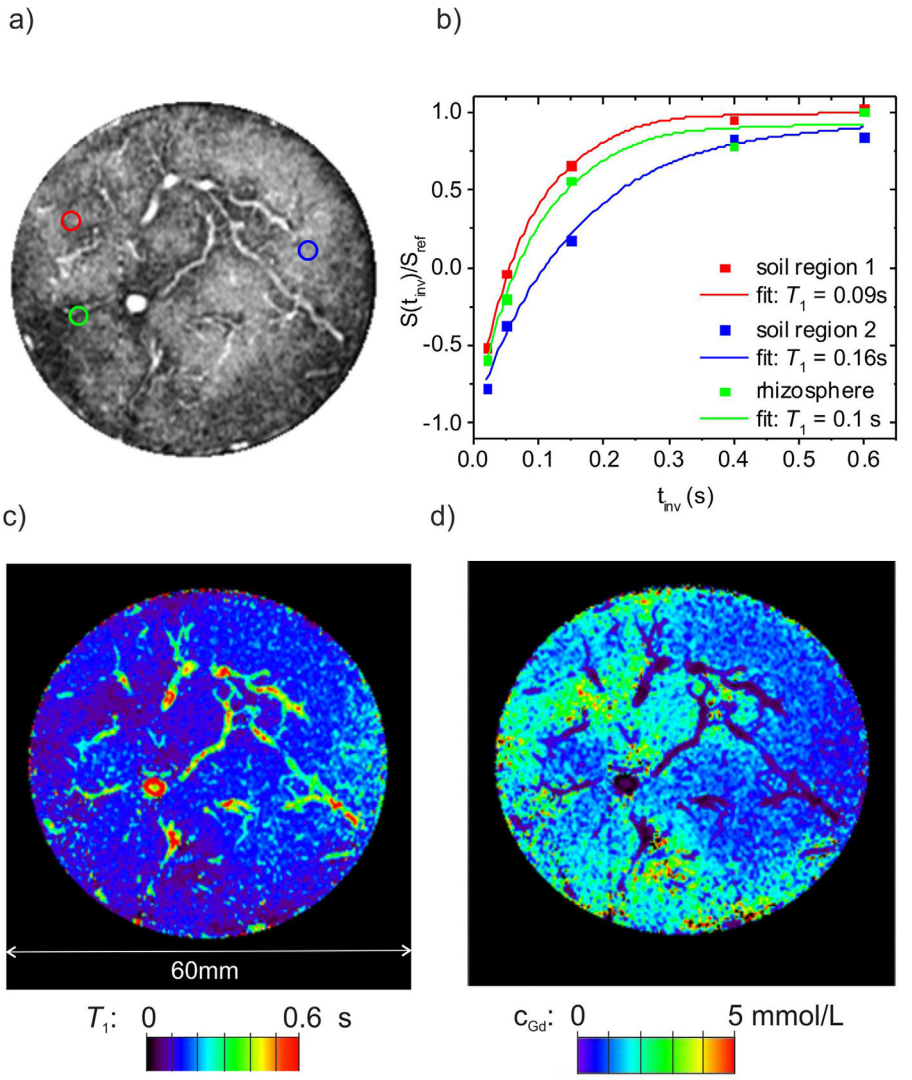

Figure 4. (a) Selected slice at 1.5 cm below the top surface from a 3D image measured with a SEMS (single echo multi slice) sequence without inversion pulse (S_{ref} image) on day 4. The colored circles mark chosen voxels to illustrate the course of $S(t_{inv})/S_{ref}$ relaxation curves obtained with the IR-SEMS (inversion recovery single echo multislice) MRI sequence. Red: soil region 1, blue: soil region 2, green: rhizosphere region. (b) Corresponding $S(t_{inv})/S_{ref}$ relaxation curves of the chosen voxels in a) and fits by using equation (5). (c) T_1 map of the selected slice. (d) Gd concentration map calculated from T_1 map in c) using equation (1).

$\theta = 0.36$ cm^{3}cm^{-3} to $\theta = 0.22$ cm^{3}cm^{-3}. Root system and T_1 maps were imaged during the night phases as described in the section "Material and Methods." One example is shown in Figure 4 for an axial slice located 1.5 cm below the top soil surface. The well-developed root system consists of a tap root with a thickness of about 3 mm and a multiplicity of lateral roots that fill the entire cuvette diameter (Figure 4a). The root system shows a higher intensity because the volumetric water content of a root is considerably larger than that of the soil and the T_2 relaxation time of water is longer in the roots than in the soil pores. Sample voxels from two places in the soil and one in the rhizosphere illustrate the change in normalized signal intensity versus inversion recovery time t_{inv} from which the T_1 relaxation time is derived (Figure 4b). The curves run as expected from -1 to $+1$ and their courses are well described by equation (5). It is worth mentioning that the accuracy of the fitted T_1 and the derived concentration are related to the distribution and the number of t_{inv}. A map of fitted T_1 for all voxels in the selected slice is shown in Figure 4c. The longitudinal relaxation times T_1 in the soil regions are mostly below 0.2 s due to the presence of Gd, whereas the roots are clearly discriminated by their slower T_1 in the range higher than 0.3 s. A more precise idea of the tracer

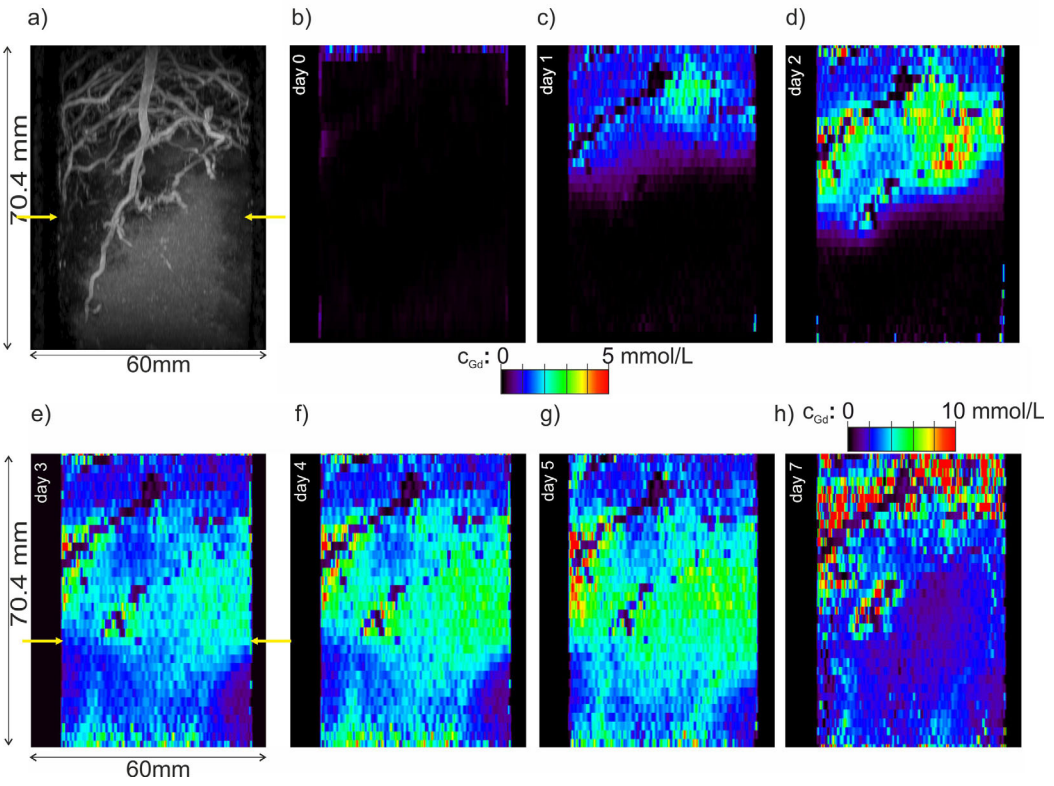

Figure 5. Infiltration of the Gd plume in the plant container. (a) Maximum intensity projection of the root system on day 7. Note that also part of the water in the sand packing is still visible, since the water content was very high, and the signal could not faded out completely by setting a threshold value. The yellow arrows indicate the approximate bottom of the root zone. (b–h) Gd concentration maps in a central vertical slice with a FOV of 60 mm × 70.4 mm, and a resolution of 0.234 mm × 2.2 mm. In the first 6 images the concentration range goes from 0 to 5 mM and is enhanced in Figure 5h for day 7 to 10 mM.

distribution is obtained from the concentration map shown in Figure 4d. Already after 4 days a distribution pattern developed which is due to both soil heterogeneity and root activity. After 4 days of tracer application, the pore water at 1.5 cm depth was replaced almost completely by the applied tracer solution since the concentrations were equal or higher than the applied tracer concentration of 1 mM. The highest concentrations of about 3–4 mM were found in the left part of the image and in the neighborhood of many roots whereas in the vicinity of some roots no increase in tracer concentration was observed. The higher tracer concentrations in the soil than in the applied tracer solution must be due to water uptake but tracer exclusion by the roots.

Figure 5 displays vertical Gd concentration maps to demonstrate the evolution of tracer infiltration and accumulation. In order to relate the concentration patterns to the root distribution, the projection of the root system is also shown in Figure 5a. Until day 1 (Figure 5c) the Gd front with $c_{Gd} \cong 1$ mM moved about 30 mm deep into the sand packing and a spot with relatively high enrichment up to $c_{Gd} \cong 2$–3 mM was already detected in the densely rooted zone. The enrichment continued during day 2 while the front moved further downward (Figure 5d). This accumulation is the consequence of water uptake by the roots, while the tracer was excluded. At the same time, the solution was also transported downward by the flow so that the accumulation patterns also moved downward. In order to keep the transpiration-to-efflux ratio constant and to compensate for the increased transpiration due to leaf development, the irrigation rate was increased from 22 mL/d to 26 mL/d after day 2. This led to a slight dilution of the enrichment plume during day 3 and 4 (Figure 5e) but after day 4 the enrichment continued.

The leaching fraction (LF) at day 5 is 0.25 (= cumulative efflux/cumulative irrigation) which implies that the expected steady state tracer concentration at the bottom of the root zone would be a factor 4 ($= LF^{-1}$) higher than the concentration of the applied water. If we define the bottom of the root zone at approximately 40 mm below the top surface of the container (see Figure 5a, yellow arrows), then we

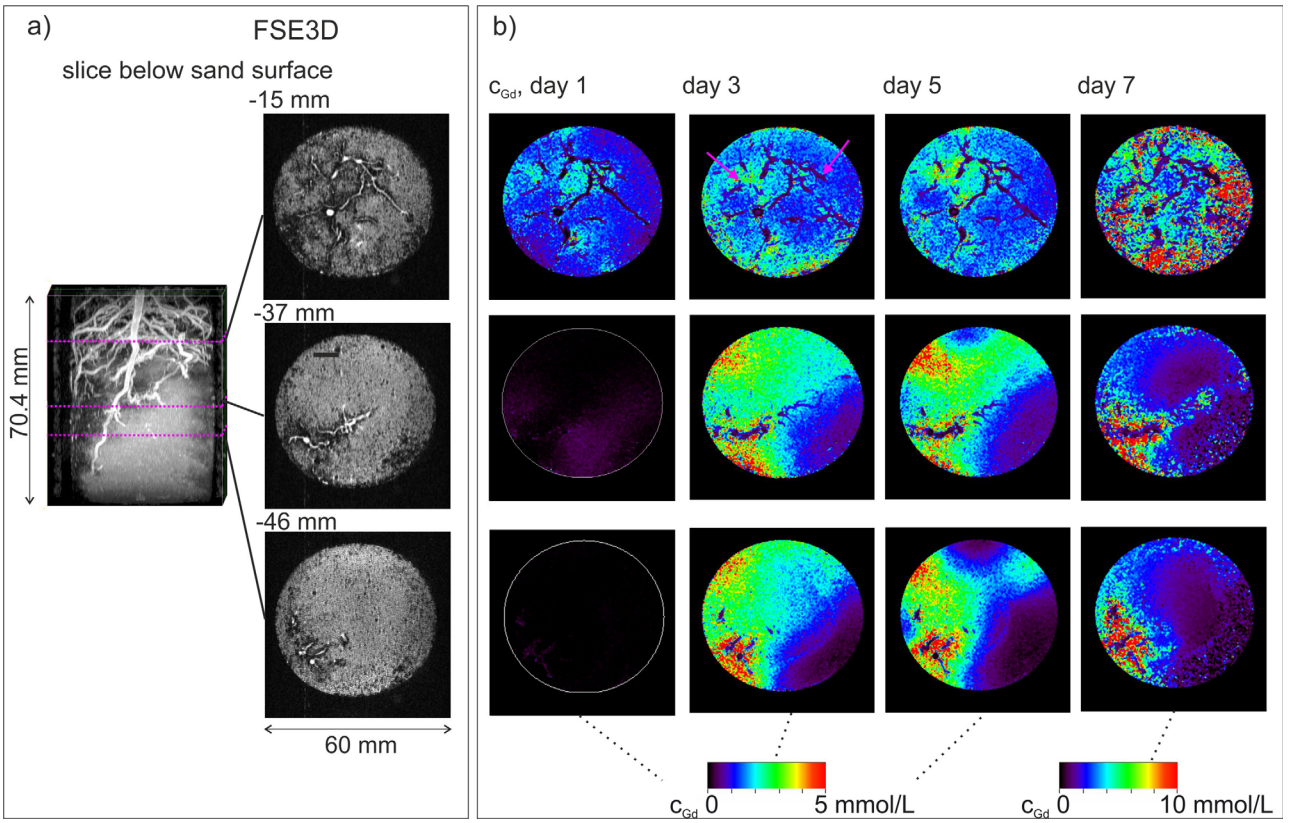

Figure 6. Exemplary axial slices from top to bottom. (a) Original FSE3D images from day 0. (b) Gd concentration maps on day 1, day 3, day 5, and day 7 after start. The arrows on day 3 indicate active and less active roots, which did not enrich GdDTPA.

observe that the steady state concentration was approximately reached at this depth at day 3. Below the root zone (< -40mm) the concentrations were still lower than at the bottom of the root zone and slightly increased with time from day 3 until day 5. Also the tracer concentrations in the effluent demonstrate the concentration in the lower part of the column were still increasing with time and did not reach the expected concentrations based on the leaching fraction, i.e., about 4 mM (see Figure 2b). But the increase in concentration was not uniform, i.e., some zones where the concentrations increased slowly seemed to be bypassed by the tracer plume (see also Figure 5g). The irrigation was terminated on day 6 but transpiration continued so that the overall concentration in the soil column increased significantly to $c_{Gd} > 10$ mM until day 7 around the roots near the top and in deeper regions (Figure 5h). These values demonstrate that the new approach extends the accessible concentration range by more than three times in comparison to the previous T_1 weighted procedure and allows to image the accumulation process completely.

The enrichment process can be monitored in more detail by inspection of a time series of selected axial slices. Figure 6a shows the full root system and parts of it in three chosen axial slices at 15 mm, 37 mm, and 46 mm below the sand surface. As mentioned already in the discussion of Figure 4 the taproot and many lateral roots are clearly discriminated from the soil. These structures are between 1 and 4 pixels thick, i.e., 0.23 mm to 1 mm. In MRI the signal results from emission of radiation from NMR active nuclei, mostly ^{1}H of the water molecule. Generally, the signal intensity is determined by both the spin density and the weighting factor depending on relaxation times. The contrast between root and soil is controlled first by the much higher water content and second by the slower relaxation times in the root. The contribution of the relaxation term can be enhanced by increasing the echo time which damps the relative contribution of the soil signal. Consequently, roots with a diameter smaller than one voxel can be reliably discriminated from the soil [*Metzner et al.*, 2015]. Concerning the question of the voxel size this is limited by the hardware configuration and typically 200 μm can be achieved.

As in the vertical slices the Gd accumulation process is displayed in the concentration maps (Figure 6b) with a resolution of 0.23 mm × 0.23 mm. This high resolution allows an unambiguous assignment of roots with enhanced Gd enrichment and roots with less or even no enrichment (see arrows). Consequently, these images point on differences in the activity of individual roots and my lead toward a differentiation into active and less active roots. Going deeper, the concentration enhancement increased and was accompanied by a simultaneous smearing of the distinct accumulation zones. However, zones of tracer accumulation were not solely located around root cross sections in the 2D horizontal planes. A zone with higher tracer concentrations in a horizontal plane may also correspond to an accumulation process that is caused by roots that are located above the horizontal cross section. The accumulation around the roots in combination with the downward leaching generated "shadows" of zones with higher concentrations below the roots. The observed smearing was due to the dispersion by the downward flow in the porous medium. It is interesting to note that these accumulation shadows disappeared when the leaching in the soil column was stopped and flow in the soil column was only caused by root water uptake. The root water uptake during the last day of the experiment redistributed the tracer distribution within the column drastically and tracer was found to accumulate at the end of the experiment at much higher concentrations in regions close to roots.

A voxel-wise validation of the imaged concentrations was not possible but the closure of the mass balance of Gd in the complex soil-root system is a measure of the quality of the concentration quantification. To check the quantification, we compared the total amount of Gd in the column obtained from the irrigation volume minus the efflux volume after m days, $n_{Gd,tot}(m)$, with the total amount of Gd found by MRI (integration over all voxels) at day m $n_{Gd,MRI}(m)$:

$$\begin{aligned} n_{Gd,\,tot}(m) &= I_{cum,m} c_{Gd,irr} - \sum_{j=1}^{m} E_j c_{Gd,eff\,j} \\ n_{Gd,\,MRI}(m) &= \theta_{av} V_{voxel} \sum_{i=1}^{n_{voxel}} c_{Gd,voxel,i}(m) \quad , \end{aligned} \tag{6}$$

where $c_{Gd,irr}$ is the concentration in the irrigation solution (1 mM), $c_{Gd,eff,j}$ is the concentration of $GdDTPA^{2-}$ in the efflux during day j (Table 1), $I_{cum,m}$ (mL) is the cumulative irrigated volume until day m, E_j (mL) is efflux volume during day j, θ_{av} is the average volumetric water content, V_{voxel} (mL) is the volume of one voxel, $c_{Gd,voxel,i}(m)$ (mM) is the concentration determined by MRI in voxel i at day m, and n_{voxel} is the total number of voxels. Figure 7 shows the good agreement of $n_{Gd,tot}(m)$ (red circles) and $n_{Gd,MRI}(m)$ (black squares) for each day j, which strongly proves the validity of the method of determine quantitative Gd concentration maps from the T_1 relaxation time maps. The error bars are calculated using the uncertainties in Gd determination by MRI as shown in Figure 3 and the propagated uncertainties in the gravimetric mass balances.

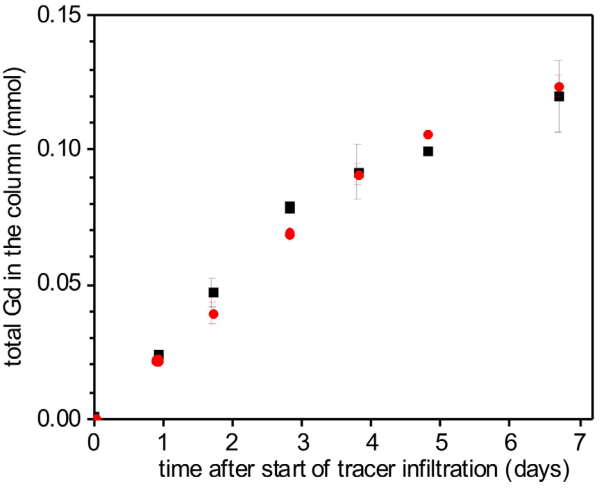

Figure 7. Comparison of gravimetrically determined total Gd in the column ($n_{Gd,\,tot}(m)$ red circles) with total Gd recovered from integration of the Gd maps over the entire volume ($n_{Gd,\,MRI}(m)$, black squares). The respective definitions are given by equation (6).

After the experiment, Gd concentrations were also measured in the plant to evaluate the Gd uptake by the plant. In Table 1, the concentrations and total Gd masses in the different parts of the plants are shown. Gd was taken up by the roots and transported to the leaves. The amount of Gd that was taken up was about 5% of the amount of Gd that was in the column at the end of the experiment. This shows that Gd can be regarded as a tracer that represents a solute that is mainly excluded by the plant roots, which is in agreement with the observed increase of the Gd concentrations in the soil.

5. Summary and Outlook

The present study showed that single echo multi slice imaging combined with inversion recovery preparation is very

convenient for quantitative detection of a T_1 reducing tracer, $GdDTPA^{2-}$, in a complex soil-root system with high spatial resolution. Compared to T_1 weighted images, using inversion recovery with different inversion times allowed direct mapping T_1 distributions from which concentration distributions could be derived. For this procedure, the highest detectable concentration depends on the shortest performable inversion time. As an example, using inversion times less than 5 ms one could determine concentrations up to 50 mM, compared to 3 mM which is the maximal concentration that can be derived from T_1 weighted images. This extended concentration range opens the possibility to observe transport and enrichment processes in the soil root systems that result from water uptake and solute exclusion by roots. The quantitative imaging procedure was validated by the mass balance of Gd in the system. In summary, MRI in combination with quantitative contrast agent determination can be a valuable tool for the investigation of solute transport and water uptake by plant roots in porous media.

Data sets of solute concentrations and their changes with progressive infiltration and transpiration could be obtained with high spatial and temporal resolution. These concentration distributions were linked to high resolution 3D images of the root system architecture. We observed that the Gd tracer was hardly taken up by the plant so that root water uptake led to an enrichment of the tracer concentrations. In future we will continue these investigations by comparing the experimental results with numerical simulations to investigate which properties of the root system (e.g., hydraulic conductance of different root types) that are linked to root water uptake and hence concentration accumulation could be inferred from these tracer concentration data. The fact that enrichment near to the root surface depends on the water flux toward the root surface and is stronger when this flux is higher opens the possibility to infer local uptake rates from tracer accumulation. However, the concurrent leaching process may blur this relation. It is therefore especially promising that concentration accumulation could also be quantified at the end of the experiment when leaching was stopped and the flow and transport pattern in the soil column was determined entirely by the distribution of the root water uptake. An optimal experimental setup to infer water uptake rates from tracer accumulation near roots still requires further investigation and could be carried out with the aid of simulations by models that simulate flow and transport in the coupled soil-root system (e.g., R-SWMS) [*Javaux et al.*, 2008].

Acknowledgments
The authors thank the Central Institute of Engineering, Electronics and Analytics (ZEA) of the Research Center Jülich for chemical analysis of Gd in plant parts and solutions, N. Schröder for helpful discussions about theoretical background of root water uptake modelling and assistance with the preparations of the experiment, and D. van Dusschoten for maintenance of the MRI scanner. S. Haber-Pohlmeier thanks German Research Foundation for financial support (DFG: TR32 and HA-6146–3/1). The image data are available as supporting information.

References

Agbogun, H. M. D., T. A. Al, and E. M. A. Hussein (2013), Three dimensional imaging of porosity and tracer concentration distributions in a dolostone sample during diffusion experiments using X-ray micro-CT, *J. Contam. Hydrol.*, *145*, 44–53, doi:10.1016/j.jconhyd.2012.11.008.

Ahmed, S., T. N. Klassen, S. Keyes, M. Daly, D. L. Jones, M. Mavrogordato, I. Sinclair, and T. Roose (2016), Imaging the interaction of roots and phosphate fertiliser granules using 4D X-ray tomography, *Plant Soil*, *401*, 125–134.

Bechtold, M., S. Haber-Pohlmeier, J. Vanderborght, A. Pohlmeier, T. P. A. Ferre, and H. Verreecken (2011), Near-surface solute redistribution during evaporation, *Geophys. Res. Lett.*, *38*, L17404, doi:10.1029/2011GL048147.

Blümich, B. (2000), *NMR Imaging of Materials*, Clarendon, Oxford, U. K.

Callaghan, P. T. (1991), *Principles of Nuclear Magnetic Resonance Microscopy*, Oxford Univ. Press, Oxford, U. K.

Daly, K. R., S. J. Mooney, M. J. Bennett, N. M. J. Crout, T. Roose, and S. R. Tracy (2015), Assessing the influence of the rhizosphere on soil hydraulic properties using X-ray computed tomography and numerical modelling, *J. Exp. Bot.*, *66*, 2305–2314, doi:10.1093/jxb/eru509.

Dara, A., A. B. Moradi, P. Vontobel, and S. Oswald (2015), Mapping compensationg root water uptake in heterogeneous soil conditions via neutron tomography, *Plant Soil*, *397*, 273–287.

de Jong van Lier, Q. D., J. C. van Dam, and K. Metselaar (2009), Root water extraction under combined water and osmotic stress, *Soil Sci. Soc. Am. J.*, *73*, 862–875, doi:10.2136/sssaj2008.0157.

Greiner, A., W. Schreiber, G. Brix, and W. Kinzelbach (1997), Magnetic resonance imaging of paramagnetic tracers in porous media: Quantification of flow and transport parameters, *Water Resour. Res.*, *33*, 1461–1473, doi:10.1029/97WR00657.

Haake, E. M., R. W. Brown, M. R. Thompson, and R. Venkatesan (1999), *Magnetic Rresonance Imaging, Physical Principles and Sequence Design*, Wiley-Liss, New York.

Haber-Pohlmeier, S., M. Bechtold, S. Stapf, and A. Pohlmeier (2010), Water flow monitored by tracer transport in natural porous media using MRI, *Vadose Zone J.*, *9*, 835–845.

Harbottle, M. J., M. D. Mantle, M. L. Johns, R. Van Herwijnen, A. Al-Tabbaa, T. R. Hutchings, A. J. Moffat, and S. K. Ouki (2007), Magnetic resonance imaging of the effect of zeolite on lithium uptake in poplar, *Environ. Sci. Technol.*, *41*, 3444–3448, doi:10.1021/es0623111.

Hupet, F., and M. Vanclooster (2002), Intraseasonal dynamics of soil moisture variability within a small agricultural maize cropped field, *J. Hydrol.*, *261*, 86–101.

Javaux, M., T. Schröder, J. Vanderborght, and H. Vereecken (2008), Use of a three-dimensional detailed modeling approach for predicting root water uptake, *Vadose Zone J.*, *7*, 1079–1088.

Jelinkova, V., M. Snehota, A. Pohlmeier, D. Van Dusschoten, and M. Cislerova (2011), Effects of entrapped residual air bubbles on tracer transport in heterogeneous soil: Magnetic Resonance Imaging Study, *Org. Geochem.*, *42*, 991–998.

Katul, G., P. Todd, D. Pataki, Z. J. Kabala, and R. Oren (1997), Soil water depletion by oak trees and the influence of root water uptake on the moisture content spatial statistics, *Water Resour. Res.*, *33*, 611–623.

Kuhlmann, A., I. Neuweiler, S. van der Zee, and R. Helmig (2012), Influence of soil structure and root water uptake strategy on unsaturated flow in heterogeneous media, *Water Resour. Res.*, *48*, W02534, doi:10.1029/2011WR010651.

Lavini, C., and J. J. C. Verhoeff (2010), Reproducibility of the gadolinium concentration measurements and of the fitting parameters of the vascular input function in the superior sagittal sinus in a patient population, *Magn. Reson. Imaging*, *28*, 1420–1430.
MacFall, J. S., and H. Van As (1996), Magnetic resonance imaging of plants, in *Nuclear Magneit Resonance in Plant Biology*, edited by Y. Shachar-Hill and P. E. Pfeffer, pp. 33–76, Plant Physiol. Soc. Am., Rockville, Md.
Manning, T. J., W. Fiskus, M. Mitchell, and L. Dees (1999), Determination of the protonation constants of Gadolinium(Iii) diethyltriaminepentaacetic acid by solvent extraction and icp-aes, *Spectrosc.Lett.*, *32*, 463–467.
McRobbie, D. W., E. A. Moore, M. J. Graves, and M. R. Prince (2007), *MRI From Picture to Proton*, Cambridge Univ. Press, Cambridge, U. K.
Metzner, R., A. Eggert, D. van Dusschoten, D. Pflugfelder, S. Gerth, U. Schurr, N. Uhlmann, and S. Jahnke (2015), Direct comparison of MRI and X-ray CT technologies for 3D imaging of root systems in soil: Potential and challlenges for root trait quentification, *Plant Methods*, *11*, 17, doi:10.1186/s13007-015-0060-z.
Moradi, A. B., S. E. Oswald, J. A. Massner, K. P. Pruessmann, B. H. Robinson, and R. Schulin (2008), Magnetic resonance imaging methods to reveal the real-time distribution of nickel in porous media, *Eur. J. Soil Sci.*, *59*, 476–485, doi:10.1111/j.1365-2389.2007.00999.x.
Moradi, A. B., S. E. Oswald, J. A. Nordmeyer-Massner, K. P. Pruessmann, B. H. Robinson, and R. Schulin (2010), Analysis of nickel concentration profiles around the roots of the hyperaccumulator plant Berkheya coddii using MRI and numerical simulations, *Plant Soil*, *328*, 291–302, doi:10.1007/s11104-009-0109-8.
Moradi, A. B., A. Carminati, D. Vetterlein, P. Vontobel, E. Lehmann, U. Weller, J. W. Hopmans, H. J. Vogel, and S. E. Oswald (2011), Three-dimensional visualization and quantification of water content in the rhizosphere, *New Phytol.*, *192*, 653–663, doi:10.1111/j.1469-8137.2011.03826.x.
Morkenborg, J., M. Pedersen, F. T. Jensen, H. Stodkilde-Jorgensen, J. C. Djurhuus, and J. Frokiaer (2003), Quantitative assessment of Gd-DTPA contrast agent from signal enhancement: An in vitro study, *Magn. Reson. Imaging*, *21*, 637–643.
Nagel, K. A., et al. (2009), Temperature responses of roots: Impact on growth, root system architecture and implications for phenotyping, *Funct. Plant Biol.*, *36*, 947–959, doi:10.1071/fp09184.
Nestle, N., A. Wunderlich, R. Niessner, and T. Baumann (2003), Spatial and temporal observations of adsorption and remobilization of heavy metal ions in a sandy aquifer matrix using magnetic resonance imaging, *Environ. Sci. Technol.*, *37*, 3972–3977.
Oswald, S., W. Kinzelbach, A. Greiner, and G. Brix (1997), Observation of flow and transport processes in artificial porous media via magnetic resonance imaging in three dimensions, *Geoderma*, *80*, 417–429.
Pohlmeier, A., A. M. Oros-Peusquens, M. Javaux, J. Lindenmair, M. I. Menzel, H. Vereecken, and N. J. Shah (2008), Changes in soil water content resulting from ricinus root uptake monitored by magnetic resonance imaging, *Vadose Zone J.*, *7*, 1010–1017.
Pohlmeier, A., D. Van Dusschoten, L. Weihermüller, U. Schurr, and H. Vereecken (2009), Imaging water fluxes in porous media by magnetic resonance imaging using D2O as a tracer, *Magn. Reson. Imaging*, *27*, 285–292.
Schlüter, S., H. J. Vogel, O. Ippisch, and J. Vanderborght (2013), Combined impact of soil heterogeneity and vegetation type on the annual water balance at the field scale, *Vadose Zone J.*, *12*, doi:10.2136/vzj2013.03.0053.
Schroeder, N., M. Javaux, J. Vanderborght, B. Steffen, and H. Vereecken (2012), Effect of root water and solute uptake on apparent soil dispersivity: A simulation study, *Vadose Zone J.*, *11*, doi:10.2136/vzj2012.0009.
Schroeder, N., N. Lazarovitch, J. Vanderborght, H. Vereecken, and M. Javaux (2014), Linking transpiration reduction to rhizosphere salinity using a 3D coupled soil-plant model, *Plant Soil*, *377*, 277–293, doi:10.1007/s11104-013-1990-8.
Segal, E., T. Kushnir, Y. Mualem, and U. Shani (2008), Microsensing of water dynamics and root distributions in sandy soils, *Vadose Zone J.*, *7*, 1018–1026, doi:10.2136/vzj2007.0121.
Teuling, A. J., and P. A. Troch (2005), Improved understanding of soil moisture variability dynamics, *Geophys. Res. Lett.*, *32*, L05404, doi:10.1029/2004GL021935.
Vereecken, H., et al. (2016), Modeling soil processes: Review, key challenges, and new perspectives, *Vadose Zone J.*, *15*, doi:10.2136/vzj2015.09.0131.
Wang, L., Y. Nakanishi, A. Hyodo, and T. Suekane (2016), Three-dimensional structure of natural convection in a porous medium: Effect of dispersion on finger structure, *Int. J. Greenhouse Gas Control*, *53*, 274–283, doi:10.1016/j.ijggc.2016.08.018.
Yoon, H., C. Zhang, C. J. Werth, and A. Valocchi (2008), Numerical simulation of water flow in three dimensional heterogeneous porous media observed in a magnetic resonance imaging experiment, *Water Resour. Res.*, *44*, W06405, doi:10.1029/2007WR006213.
Zarebanadkouki, M., Y. X. Kim, A. B. Moradi, H. J. Vogel, A. Kaestner, and A. Carminati (2012), Quantification and modeling of local root water uptake using neutron radiography and deuterated water, *Vadose Zone J.*, *11*, doi:10.2136/vzj2011.0196.
Zarebanadkouki, M., Y. X. Kim, and A. Carminati (2013), Where do roots take up water? Neutron radiography of water flow into the roots of transpiring plants growing in soil, *New Phytol.*, *199*, 1034–1044, doi:10.1111/nph.12330.
Zarebanadkouki, M., E. Kroener, A. Kaestner, and A. Carminati (2014), Visualization of root water uptake: Quantification of deuterated water transport in roots using neutron radiography and numerical modeling, *Plant Physiol.*, *166*, 487–499, doi:10.1104/pp.114.243212.
Zarebanadkouki, M., F. Meunier, V. Couvreur, J. Cesar, M. Javaux, and A. Carminati (2016), Estimation of the hydraulic conductivities of lupine roots by inverse modelling of high-resolution measurements of root water uptake, *Ann. Bot.*, *118*, 853–864, doi:10.1093/aob/mcw154.